Supporting Information

SI Materials and Methods

Cell Culture. Adherent growing human foreskin diploid fibroblasts (HCA2) were cultivated in minimum essential medium (MEM) alpha (Invitrogen Inc.), supplemented with 10% fetal bovine serum. Human mammary epithelial cells, MCF10A obtained from ATCC, were grown in MEMB media supplemented with bovine pituitatry hormone (13 mg/mL), hydrocortisone (0.5 mg/mL), hEGF (10 μg/mL), insulin (5 mg/mL), and cholera toxin (100 ng/mL) (Invitrogen Inc.). Both cell lines were grown at 37 °C, with 95% humidity and 5% CO_2. For experiments, both cell lines were seeded either in Permanox plastic 8-well Lab-Tek chamber slides (Nalge Nunc International Corporation) or on 48 hydrophilic spots of functionalized glass-slides (AmpliGrid, Beckman Coulter GmbH). The cells were grown to a confluent layer prior to irradiation. HT1080 and human bronchial epithelial cells (HBEC) were grown and maintained as previously described (1). For live cell imaging, HT1080 and HBEC were stably transfected with 53BP1-GFP (1), whereas MCF10A were transiently transfected with H1.5-DsRed2 and 53BP1-GFP using lipofectamine LTX (Invitrogen). H1.5-DsRed2 for chromatin labeling was generously given by Michael Hendzel from the University of Alberta, Canada. DNA damage labeling was done with 53BP1-GFP construct, generously given by Thanos Halazonetis from the University of Geneva, Switzerland.

Irradiation. Identical dose- and time-response experiments were conducted with cells exposed to X-rays (160 or 320 kV) to optimize the immunostaining of radiation-induced foci. For the optimization experiments, cells were irradiated with 100 cGy of X-ray and fixed after 30-min repair time to get a maximum radiation-induced foci (RIF) induction as previously shown (2). For the matrix experiments with different doses and time responses, cells grown on one functionalized glass slide were irradiated with two doses. Therefore, one part of the modified glass slide was shielded with lead. Furthermore, the sample was placed on top of lead to minimize backscattering. Cells in each well were fixed at different time and dose points (0, 1, 5, 10, 20, 40, 80 min post-IR/0, 5,10, 15, 40, 50, 100, 200, and 400 cGy) on a warm block and returned to the 37 °C incubator. Dose rates were modified as little as possible for each dose as long as the exposure time was less than 1 min to get accurate early time points, and was more than 10 s for accurate determination of the dose. This led to three different dose rates: 450 cGy/min for 200 and 400 cGy; 150 cGy/min for 100, 50, and 40; 30 cGy/min for 5, 10, and 15 cGy. For high-LET radiation, cells were irradiated at the accelerator beam line of the National Aeronautics and Space Administration Space Research Laboratory at Brookhaven National Laboratory, with either 1 GeV/atomic mass unit Fe ions or 1 GeV/atomic mass unit O ions (LET = 150 keV/μm and 14 keV/μm, respectively). A dose of 1 Gy was delivered at a dose rate of 100 cGy/min.

Immunostaining. Two different culture platforms were evaluated (i.e., 48-microwell ampligrid vs. 8-well chamber slides). Immunostaining was optimized using cells exposed to 100 cGy of X-rays and fixed 30 min after irradiation with 2% paraformaldehyde in PBS for 15 min at room temperature followed by permeabilization with 100% ice-cold methanol for 15 min at −20 °C. Subsequently, blocking, primary antibody incubation, and secondary antibody incubation were optimized through titration experiments. The rest of the staining was performed according to the conventional staining protocol (2) but with BSA used for blocking instead of casein supernatant. When cells were grown on Ampli-Grids, optimization was performed reducing the immunostaining time to less than 1 h. By using 5 μL of reagent for each incubation step in the microwells, we could increase antibody concentration with no significant impact on cost. Briefly, titration times for the optimization were 1, 2, 4, 8, 16, 32, or 64 min as well as additional 128 min for the primary antibody. The primary antibodies were either a rabbit polyclonal anti 53BP1 antibody (stock at 1 mg/mL, Bethyl Laboratories) or a mouse monoclonal to phosphohistone H2AX antibody (stock at 1 mg/mL, clone JBW301; Upstate Cell Signalling Solutions Inc.). The corresponding secondary antibodies were either FITC labeled antirabbit IgGs or, FITC or T-Red labeled antimouse IgGs (Molecular Probes Invitrogen). After three washing steps with PBS at room temperature, cells were either blocked with 0, 1% BSA for 1 h for the antibody titers or the blocking titer was performed with 0,1%, 0,2%, and 1% BSA at room temperature. The samples of the blocking titer were incubated with the primary antibody for 2 h and then, after extensive washing with PBS, incubated with the secondary antibody for 1 h. The other samples were either incubated with the primary antibody for 2 h and, subsequently, used for the secondary antibody titer, or the primary titer with the dilutions 1:10, 1:100, 1:200 was performed at room temperature. The primary titer samples were washed extensively with PBS after the titration and then incubated with the secondary antibody for 1 h. The secondary antibody titer samples were also washed with PBS before the secondary antibody titration was performed. Dilutions used for the secondary antibody incubation optimization were 1:10, 1:100, 1:200. After a further washing step with PBS, the samples were counterstained with DAPI and then analyzed with regard to foci intensity.

By plotting the relative foci intensities against time, saturation of the relative foci intensities was observed after a short time for all concentrations and dilutions. Saturation was reached for the blocking titration between 8–16 min in dependence on the BSA concentration. For the primary antibody, the saturation was always reached after 16 min independent from the antibody concentration. The secondary antibody plot showed more variations in the saturation time points in dependence on the antibody concentration. Saturation was obtained after 32 min for the 1:200 antibody dilutions, after 16 min for the 1:100 dilution, and after 8 min for the 1:10 dilution. Fig. S7A shows the progression of the curves for the 1:100 dilution for both antibodies and the curve for the 1% BSA solution. The curve progressions as well as the intensity of the microscopic images led to the conclusion that longer incubation does not improve the quality of the images. Indeed, longer blocking results in lower foci intensities (Fig. S7B). For both antibodies, the saturation in the foci intensity can also be seen in the microscopic images (Fig. S7 C and D). The saturation of the titration curves observed as well as the quality of the images led to the decision to reduce the incubation time for the three staining steps to 15 min for the three reagents and to use a 0.2% concentration of BSA and 1:100 dilutions for both antibodies in the matrix experiments. Corresponding images for these incubation times and dilution are shown in Fig. S7E, clearly showing the improvement in image quality compared to other conditions (Fig. S7 B–D).

Image Acquisition. Cells were viewed and imaged using a Zeiss Axiovert 200M automated microscope with Ludl position-encoded scanning stage (Carl Zeiss). Images were acquired using a Zeiss plan-apochromat 40X dry objective (N.A. of 0.95) and a

very sensitive scientific-grade EM-CCD camera (Hamamatsu C9100-02, 1,000 by 1,000 pixels, , 8×8 μm^2 pixels). The image pixel size was measured to be 0.2 μm but based on the NA of the objective, the actual resolution of the image in the FITC channel is approximately $0.5 \times 0.488/NA = 0.26$ μm. All images were captured with the same exposure time so that intensities were within the 16-bit linear range and could be compared between specimens. For 3D dataset, a CSU-10 spinning disk confocal scanner was used to acquire optical slices of 0.5-μm thickness, and illumination was provided by four solid-state lasers at 405, 491, 561, and 638 nm under AOTF control (Acousto-Optic Tunable Filters). For 2D dataset, simple conventional image was taken with the same optics but without spinning disk. Finally, a multi-band dichroic and single-band emission filters in a filterwheel selected the fluorescent light captured by the camera, removing any type of bleedthrough between channels. For X-ray experiments on live HT1080, time-lapse imaging was carried out as previously described (1), using an LSM 510 Meta laser scanning confocal microscope (Carl Zeiss) with a 63X 1.4 NA Plan-Apochromat oil immersion objective.

Cell Cycle Considerations. We noted that MCF10A are not fully arrested at confluence, and thus we corrected for high foci count from cells in G2 or S phase as previously described (2): Briefly, foci counts were scaled to represent the number of foci for the same size nucleus, using the G1 nuclear volume as the reference nuclear volume. DAPI content and EdU pulsing (Click-iT®, Invitrogen) were used to estimate proportions of cells in each phase. Note that cells in late G2 are problematic as 53BP1 signals becomes weaker with a signal fully cytoplasmic during mitosis, leading to complete loss of foci until reentry in G1. However, this effect should have very little impact on the analysis because only 5% of cells were in G2 and less than 1% in mitosis. We also measured 9% of the cells being in S phase, which could lead to higher foci background due to stalled replication forks. However, working with 53BP1 alleviated this problem, as background issues have been reported primarily with γH2AX not 53BP1 (2).

Image Analysis of Live Cells. Processing of 3D time lapse was done by first applying a maximum intensity projection (MIP) on all Z stack to allow visualization of all foci within one single plane. This first step resulted in the generation of 2D time lapse, which could then be realigned between time points on a per nucleus basis (translation and rotation), to help distinguishing foci movement from foci formation or resolution. Various doses of X-rays were considered (0.05, 0.1, and 1 Gy) for a kinetic covering 5 min to 20 h post-IR, depending on the cells used. 3D time lapses were acquired and averaged over 20 and 40 cells for each dose. RIF size for live cell imaging was obtained by computing the full width at half maximum determined by a 1D intensity profile crossing the center of the RIF. The cross-section was done manually, and the reported size only reflected the average diameter of the RIF.

Impact of Foci Size and Foci Density on Foci Detection. Nuclear space occupied by RIF was identified by applying a constant threshold on the wavelet filtered image, and watershed algorithm was used to separate touching RIF. To test if focus size could affect the accuracy of automatic RIF detection, we applied the software on simulated data where foci sizes and densities had different values (i.e., 1 to 40 foci/nucleus were simulated with four distinct sizes: 0.1, 0.4, 1.3, and 2.4 μm^3, Fig. S8). We concluded that foci overlap

at the highest foci density (40 foci/nucleus) will be negligible in real data and therefore will not impact RIF counts. When foci were all as large as 1.3 or 2.4 μm^3, we started computing number of foci/nucleus lower than simulated (i.e., 10% and 25% lower than expected, respectively, when simulating 40 foci/nucleus). It is interesting to note in that situation the algorithm reported lower sizes than simulated as well. This reflects the ability of the algorithm to separate touching foci, minimizing the impact of foci overlap. Because RIF sizes are on average much lower (i.e., 95% of RIF sizes in a real specimen exposed to 1 Gy are below 1 μm^3; Fig. S8A), and the minimum detectable focus size is approximately 0.1 μm^3, simulations suggest that foci overlap at the highest foci density (40 foci/nucleus) will be negligible in real data and therefore will not impact RIF counts. For quantification of RIF in live cells, we counted both the cumulative and instantaneous number of RIF manually in 3D time-lapse images. Time interval varied between experiments and was generally set to 10 min interval for the first hour, followed by 30 min interval afterward. This setting was optimum to minimize phototoxicity and specimen bleaching. Because of the difficulty of software to track individual foci in successive time lapse, analysis was done manually in a blind manner on processed images.

Background Foci Correction. The human cells we used have significant amount of background foci. In this work, we introduced a method to correct for their presence in irradiated specimen. Briefly, we know that DNA damages are random events taking place in a specified unit of space (the nucleus) with an average frequency Φ (RIF/nucleus). Therefore, the probability of having N hits in a given cell is defined by the Poisson distribution $Pois(N,\Phi)$. If we were to measure the number of cells with N RIF after exposure of a dose D, this would lead to the distribution $H(N,D) = H(N,0) \otimes Pois(N,\Phi)$, where $H(N,0)$ is the distribution of background foci without radiation. In other words, the measured distribution of RIF/nucleus in a specimen should be a Poisson distribution whose means is the average number of RIF/nucleus convolved with the distribution of background foci present before exposure to ionizing radiation. For each measured distribution $H(N,D)$, we searched the value of Φ that yielded the best fit by incremental changes on Φ.

If the Poisson assumption is right, such method should lead to more accurate values for RIF estimation (i.e., fitting with a mathematical function is less sensitive to noise than computing the average). High R squared values between the fits and the measured distributions were indeed observed (average $R^2 \sim 0.92$; Fig. S9), validating the assumption that "real" RIF are distributed randomly among nuclei, much like double strand break (DSB). This background correction worked well down to 0.15 Gy (average $R^2 \sim 0.93$). However, 0.05 Gy exposures led to distributions that could not be fitted with high statistical significance, a problem that might be overcome with much larger sample sizes. We are, therefore, only reporting RIF frequencies for doses ≥0.15 Gy. One should also note that correcting the measured number of RIF by only subtracting the mean number of background foci could not have been fitted well by a Poisson distribution due to the non-Poisson contribution of background foci (green curve, Fig. S9, *Upper*). It is known that background foci changes with each cell cycle and the nonnormal distribution probably reflects the various cycle distribution. Therefore, such traditional method would not have permitted us to conclude on the random distribution of RIF.

1. Asaithamby A, Chen DJ (2009) Cellular responses to DNA double-strand breaks after low-dose gamma-irradiation. *Nucleic Acids Res* 37:3912–3923.

2. Costes SV, et al. (2006) Imaging features that discriminate between foci induced by high- and low-LET radiation in human fibroblasts. *Radiat Res* 165:505–515.

Fig. S1. Time-lapse imaging of human fibrosarcoma HT1080 stably transfected with 53BP1-GFP. (*Upper*) Representative snapshots of movies for three different doses (5, 10, and 100 cGy). Counting was done manually and done in two different ways: (*i*) static measurement, indicating the number of RIF/cell at the time it is measured (green numbers and graphs); (*ii*) cumulated measurement, indicating at any time the overall number of different RIF that have appeared since time 0 (red numbers and graphs). (*Lower*) The average of these counts from 20–40 nuclei per dose (red square for cumulated averages and green triangles for static averages). Static and cumulated averages could be fitted simultaneously with the same parameters using Eqs. **1** and **2**, respectively.

Fig. S2. Human validation of spot detection algorithm. Human mammary epithelial cells (MCF10A) were exposed to various doses of X-rays, immunostained for 53BP1, and RIF were counted manually or by algorithm from 3D stacks. Graph plotting RIF counts scored by computer algorithm against RIF counts scored blindly by human eye for various doses show good agreement. A total of 350 nuclei were scored here, and each nuclear count is represented as a circle, with circles of larger sizes for larger doses. Linear regression led to an overall $R^2 = 0.88$ and P value for t test less than 0.05 (lower graph), indicating good agreement between manual and automatic counts.

Fig. S3. RIF dose-kinetic fits from single experiment performed on normal human skin diploid fibroblasts in G1 (HCA2) imaged by 3D microscopy and stained for 53BP1. (*A*) Absolute RIF yield α (RIF/Gy per nucleus), showing a decrease with dose. (*B*) RIF induction kinetics constants (k_1), showing a faster induction with dose. (*C*) RIF disappearance-resolution kinetics constants (k_2) showing a slower RIF resolution with dose. Note that because only one experiment was performed here, error bars represent standard deviations from measurements made over 3,000 nuclei per dose point. Trend significance using *t* test between [0.1, 0.4] Gy group and high dose group and using duplicate well as separate measurements ($P < 0.05$) are shown by asterisk.

Fig. S4. Illustration of energy deposition from HZE particle 1 GeV/atomic mass unit Fe ion in a theoretical rectangular cell. A small red cylinder crossing the cell in the middle along its length indicates the core of the HZE. Delta rays generated in the core via Coulomb interactions are depicted as green arrows.

Fig. S5. Time-lapse imaging of MCF10A exposed to 1 track of 1 GeV/atomic mass unit Fe ion (approximately 0.24 Gy, LET ~ 148 keV/μm). Cells are transiently transfected with 53BP1-GFP RIF and H3-dsRed. Time-lapse confirms delayed kinetics for the apparition of low-LET RIF (appearing delta-rays RIF are indicated by blue arrows in each time frame). Track RIF frequency here is approximately 0.65 RIF/μm across the time points 11 to 30 min post-IR, whereas low-LET RIF frequencies reach a maximum between 24 and 30 min post-IR.
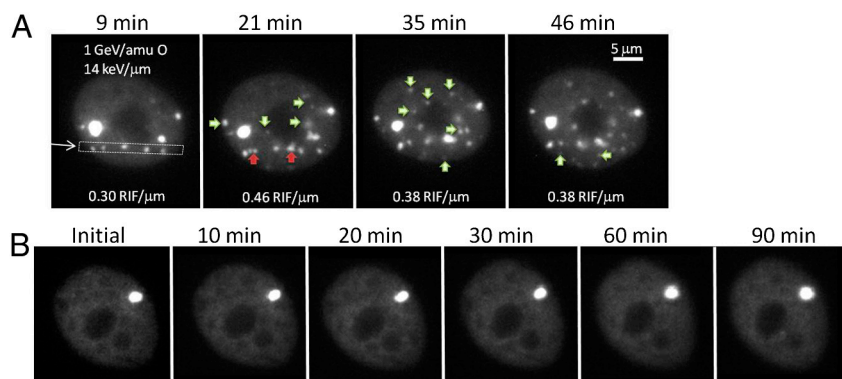
Fig. S6. (A) Stably transfected human bronchial epithelial cells (HBEC) exposed to 1 track of 1 GeV/atomic mass unit O ions (approximately 0.022 Gy, LET ~ 14 keV/μm). (B) Control HBEC, which did not get irradiated, show no induction of foci for similar time-lapse acquisition frequency. This confirms that delayed foci appearing in A are not the result of photodamage from imaging.

Fig. S7. Immunofluorescence (IF) staining optimization. Optimization of 53BP1 staining was performed for the concentrations and incubation times of three parameters: (*i*) the blocking agent (BSA), (*ii*) the primary antibody (1° Ab), and (*iii*) the secondary antibody (2° Ab). The unoptimized staining protocol was blocking with 0.1% BSA (1 h), incubation with 1° Ab (1:200, 1 h) and 2° Ab (1:200, 2 h). (*A*) IF intensities of 53BP1 staining for various incubation times of the 1° and 2° Ab (using optimized Ab concentrations). The relative foci intensities saturate for all conditions after about 16 min. This indicates short incubation times (approximately 15–20 min), with higher concentrations of Ab (1:100) is enough for optimum results. This conclusion is supported by visual analysis of the microscopic images, as is the effect of combining each optimized parameter, which appears additive (*B–E*). (*F*) Picture of an ampligrid slide (reprinted, with permission from Beckman Coulter).

A

0.15

<V>~0.45 µm³

0.1

0.05

5% of all RIF

0

0   0.5   1   1.5   2

Focus volume, V (µm³)

B

<V>~0.45 µm³

N~30

MCF10A, 2Gy, 20 min

Real data

C

Measured # of foci/nuc

40

30

20

10

0

0   10   20   30   40

Real # of foci/nuc

D

Measured foci volume V (µm³)

2.5

2

1.5

1

0.5

0

0   10   20   30   40

Real # of foci/nuc

○ 0.1 µm³
○ 0.4 µm³
○ 1.3 µm³
○ 2.4 µm³

E

σ=1   V=0.1 µm³   σ=2   V=0.4 µm³   σ=3   V=1.3 µm³   σ=4   V=2.4 µm³

N~40, 100%   N~38, 95%   N~34, 85%   N~30, 75%

$RandSpot \otimes GaussF(\sigma)$

Artificial data

Fig. S8. Impact of foci sizes on detection. (*A*) Distribution of 53BP1 RIF volumes after 2 Gy of X-rays in MCF10A. (*B*) Representative MIP is shown below the graph. The average focus volume for this time point is 0.45 µm³. The distribution indicates that 95% of RIF have volumes lower than 1 µm³. (*C*–*E*) Using the same set of nuclei, random spots were generated in the 3D volumes defined by each nucleus from an average of 1 to 40 foci/nucleus. The same spots were expanded using a Gaussian filter with various sigma values ($\sigma = 1, 2, 3, 4$) leading to various foci volumes (0.1, 0.4, 1.3, and 2.4 µm³, respectively). The position of each of this foci volumes are depicted with the same color on the distribution graph in *A*—except 2.4 µm³, which is off the chart. (*C*) For 1.3 and 2.4 µm³ foci, detection is statistically lower than reality when the average number of foci/nucleus is greater than 30 and 20, respectively. (*D*) The reported foci volume as a function of the number of foci/nucleus for different simulated foci volumes. One can note that the algorithm can maintain accurate count by reducing the reported volume of the foci. (*E*) MIP of the corresponding images for these different expansions.

Fig. S9. Background correction. The number of RIF/nucleus for each time point following two doses (0.15 and 2 Gy) in MCF10A labeled with 53BP1 were corrected for background level of background foci. Counts distribution for RIF/nucleus are shown as histogram [H(Dose)] and fitted by a Poisson distribution of mean M(POIS(M)) convolved with the foci/nucleus distribution of unirradiated specimen (green curve, *Top*, H(0 Gy)). The mean M that led to the best fit, which is displayed over each histogram as a blue solid line, corresponds to the reported real RIF yield for a given time point corrected for background foci. As one would expect, these graphs confirm that the number of real RIF/nucleus follow a Poisson distribution much like the number of DSB/nucleus.